



UNIVERSITY OF LEEDS

This is a repository copy of *Martian Meteoric Mg⁺: Atmospheric Distribution and Variability From MAVEN/IUVS*.

White Rose Research Online URL for this paper:

<https://eprints.whiterose.ac.uk/195029/>

Version: Published Version

Article:

Crismani, MMJ, Tyo, RM, Schneider, NM et al. (7 more authors) (2023) Martian Meteoric Mg⁺: Atmospheric Distribution and Variability From MAVEN/IUVS. *Journal of Geophysical Research*, 128 (1). e2022JE007315. ISSN 2169-9097

<https://doi.org/10.1029/2022je007315>

© 2023. American Geophysical Union. All Rights Reserved. Reproduced in accordance with the publisher's self-archiving policy.

Reuse

Items deposited in White Rose Research Online are protected by copyright, with all rights reserved unless indicated otherwise. They may be downloaded and/or printed for private study, or other acts as permitted by national copyright laws. The publisher or other rights holders may allow further reproduction and re-use of the full text version. This is indicated by the licence information on the White Rose Research Online record for the item.

Takedown

If you consider content in White Rose Research Online to be in breach of UK law, please notify us by emailing eprints@whiterose.ac.uk including the URL of the record and the reason for the withdrawal request.



eprints@whiterose.ac.uk
<https://eprints.whiterose.ac.uk/>

Martian Meteoric Mg⁺: Atmospheric Distribution and Variability From MAVEN/IUVS

M. M. J. Crismani¹ , R. M. Tyo¹, N. M. Schneider² , J. M. C. Plane³ , W. Feng^{3,4} ,
J. D. Carrillo-Sánchez^{5,6} , G. L. Villanueva⁵ , S. Jain² , J. Deighan² , and S. Curry⁷ 

¹Department of Physics, California State University, San Bernardino, CA, USA, ²Laboratory for Atmospheric and Space Physics, Boulder, CO, USA, ³School of Chemistry, University of Leeds, Leeds, UK, ⁴National Centre for Atmospheric Science, University of Leeds, Leeds, UK, ⁵NASA Goddard Space Flight Center, Greenbelt, MD, USA, ⁶Department of Physics, Catholic University of America, Washington, DC, USA, ⁷Space Sciences Laboratory, Berkeley, CA, USA

Key Points:

- Eight Earth years of Mars Atmosphere and Volatile Evolution/Imaging Ultraviolet Spectrograph observations show that Mars' persistent meteoric metal ion layer is more dynamic than initially assumed
- Mg⁺ layer peak altitude, abundance, and top and bottom side slopes vary significantly over the observed time period
- The relative absence of northern hemispheric Mg⁺ during southern summer is surprising and may be related to lower atmospheric dust loading

Supporting Information:

Supporting Information may be found in the online version of this article.

Correspondence to:

M. M. J. Crismani,
matteo.crismani@csusb.edu

Citation:

Crismani, M. M. J., Tyo, R. M., Schneider, N. M., Plane, J. M. C., Feng, W., Carrillo-Sánchez, J. D., et al. (2023). Martian meteoric Mg⁺: Atmospheric distribution and variability from MAVEN/IUVS. *Journal of Geophysical Research: Planets*, 128, e2022JE007315. <https://doi.org/10.1029/2022JE007315>

Received 20 APR 2022
Accepted 23 DEC 2022

Author Contributions:

Project Administration: S. Curry

Abstract Since the discovery of atmospheric Mg⁺ on Mars in 2015 by the Mars Atmosphere and Volatile Evolution mission, there have been almost continuous observations of this meteoric ion layer in a variety of seasons, local times, and latitudes. Here, we present the most comprehensive set of observations of the persistent metal ion layer at Mars, constructing the first grand composite maps from pooled medians of subsamples of a metallic ion species. These maps demonstrate that Mg⁺ appears in almost all conditions when illuminated, with peak density values varying between 100 and 500 cm⁻³, dependent on season and local time. There exists significant latitudinal variation within a given season, indicating that Mg⁺ is not simply an inert tracer, but may instead be influenced by the meteoric input distribution and/or atmospheric dynamics and chemistry. Geographic maps of Mg⁺ density as a function of latitude and longitude indicate the influence of atmospheric tides, and there is no apparent correlation with remnant crustal magnetic fields. This work also presents counter-intuitive results, such as a reduction of Mg⁺ ions in the northern hemisphere during Northern Winter in an apparent correlation with dust aerosols.

Plain Language Summary Metallic atoms in a planet's atmosphere are present when interplanetary dust particles burn up, releasing atomic species not typically found in the lower atmosphere. The discovery of a high altitude metallic layer on Mars in 2015 has led to continued monitoring in a variety of seasons across the entire planet. These results demonstrate that this magnesium ion (Mg⁺) layer appears throughout the year, with variations in peak abundances and layer heights, due to interactions with the background atmosphere. These variations track the dynamics of the middle atmosphere, providing insight into global climate patterns and may inform our understanding of seasonal deposition of interplanetary dust particles and their sources. This first-order analysis supports future modeling efforts and provides model challenges to be understood, both of which can be explored in detail with time varying full planet climate modeling.

1. Introduction

The NASA Mars Atmosphere and Volatile Evolution's (MAVEN) Imaging Ultraviolet Spectrograph (IUVS) (McClintock et al., 2015) observes Martian atmospheric molecules, atoms, and ions since its orbital insertion in 2014. This instrument observes in the far and middle UV range (110–190 and 190–340 nm), measuring atmospheric emissions from H, the dissociation and ionization products of CO₂, atomic, and molecular species such as O and N₂, as well as meteoric ions and neutrals. While MAVEN's primary mission was intended to study the upper atmosphere and atmospheric escape to space (Jakosky et al., 2015, 2018), it has been able to study a variety of additional important phenomena, from the development of twilight cloud bands and high altitude aerosol layers (Connour et al., 2020; Jiang et al., 2019; Stevens et al., 2017), mapping three different varieties of aurora (Deighan et al., 2018; Schneider, Deighan, Jain, et al., 2015; Schneider et al., 2018) and helping to characterize the role of tides in the Martian atmosphere (Lo et al., 2015; Schneider et al., 2020). However, the unexpected discovery of meteoric ions, both from Comet Siding Spring (M. M. J. Crismani et al., 2018; Schneider, Deighan, Stewart, et al., 2015) and interplanetary dust particles as a persistent background (M. M. J. Crismani et al., 2017) has led to novel chemical schemes in the mesosphere and posed new challenges for models.

Ablation, the thermal release of ions and atoms from their original minerals, occurs in planetary atmospheres when interplanetary dust particles at orbital velocities hypersonically collide with atmospheric gases. This causes

melting, vaporization, and the subsequent release of ingrained metallic atoms (e.g., Mg, Fe, and Na) into the upper atmosphere (Plane, 1991). Ablation of the primarily metallic species typically occurs at an altitude where the pressure is ~ 1 μ bar, between 60 and 100 km (Plane et al., 2017), where entry speeds for particles in prograde and retrograde orbits range between 5.5 and 59.5 km s⁻¹ at Mars for Jupiter Family Comet and Asteroidal sources as slow particles whose average velocities are closer to the escape velocity of the planet and long-period comet particles are mainly populated by particles in retrograde orbits (Carrillo-Sánchez et al., 2020). Terrestrial metallic species have been previously studied, both to understand the ablation chemistry and as a way to investigate mesospheric dynamics (see (Plane et al., 2015) for a detailed summary). Metallic ions and neutrals (Mg, Fe, and Na) have been observed both during comet Siding Spring and thereafter in a persistent layer in reduced quantities (Benna et al., 2015; Grebowsky et al., 2017) as the MAVEN-Neutral Gas and Ion Mass Spectrometer (NGIMS) instrument samples are several scale heights (140 km and higher) above the peak of the layer.

Metallic atoms charge exchange with ambient molecular ions (particularly O₂⁺) to form atomic metal ions; a fraction also ionizes through hyperthermal collisions with air molecules during ablation, recombines with free electrons, and undergoes other chemical reactions. Subsequent chemical processing of the Mg atoms and ions occurs, where charge exchange with ambient ions produces Mg⁺ and electron recombination produces neutral Mg, with chemical loss of the metal species through the formation of meteoric smoke, potentially leading to mesospheric cloud nucleation (Plane et al., 2018). The chemical pathway that may lead to mesospheric cloud formation arose from an attempt to understand the absence of neutral Mg, observable by IUVS yet not seen in the Martian atmosphere, relying on the presence of water vapor to form large Mg-carbonates that permit cloud nucleation at higher temperatures than traditional formation schemes (Plane et al., 2018).

The density of atmospheric metallic ions is dependent on the fluence of sporadic meteors, which is modeled by a Meteoric Input Function (MIF; Carrillo-Sánchez et al., 2020; Janches et al., 2020), laboratory-measured ablation fractions as well as ionization and chemical reaction rates (Bones et al., 2016; Martín et al., 2017; Plane et al., 2015). The lifetime of Mg⁺ with respect to neutralization is 1–2 orders of magnitude higher than other ambient molecular ions (\sim hours/days compared to minutes (Plane et al., 2018; Whalley & Plane, 2010)), which permits Mg⁺ to trace atmospheric dynamics where observable. Transport processes such as advection, horizontal transport, etc. simultaneously serve to redistribute the metal ions as seen in the comet Siding Spring shower (Benna et al., 2015; M. M. J. Crismani et al., 2018; Schneider, Deighan, Jain, et al., 2015), and these dynamic effects are not readily separated without a Global Circulation Model (GCM) that includes meteoric ion chemistry.

2. Observations and Data Analysis

The MAVEN spacecraft has a uniquely elliptical orbit that benefits from atmospheric drag and subsequent fuel burns to change the location of the periapse in latitude and local time. Over the course of more than seven Earth years, MAVEN has been able to observe a variety of Martian seasons, geographic latitudes and longitudes, as well as local times. During the orbital periapse segment, the spacecraft descends through the upper atmosphere (down to 140–160 km) so that in situ measurements of atmospheric atoms and ions, as well as ambient E and B fields can be measured throughout. This spacecraft orbital geometry provides coverage of local times, solar zenith angles (SZAs), and full longitude coverage over about 4–5 orbits (each orbit is ~ 5 hr). IUVS is able to create vertical profiles during its periapse orbital segment when the instrument is oriented orthogonally to the motion of the spacecraft. Using the Mid-UltraViolet (MUV) resonant fluorescent scattering of MgII at 285 nm, IUVS investigates the abundance and structure of this meteoric ion above 60 km, where scattered solar light serves to limit the lowest altitudes from observation. In this work, we present the first global results of near continuous monitoring of Mg⁺ at Mars with implications for the formation of mesospheric cloud nuclei (Hartwick et al., 2019; Plane et al., 2018) and to provide the first constraints on a seasonally varying meteor input function MIF (Carrillo-Sánchez et al., 2020; Janches et al., 2020). As has been successfully accomplished at Earth (Feng et al., 2013; Langowski et al., 2015), this global view on meteoric ions also permits a direct investigation of the upper atmosphere, where the dynamics and chemistry can be constrained with a novel set of observations.

2.1. Observing Geometry

IUVS has varying observation modes for each orbit segment of the MAVEN; however, to retrieve meteoric ion abundances, only the limb-sounding segments are utilized as nadir measurements lack the necessary limb

enhancement factor for this trace species (Chamberlain & Hunten, 1990). For this work, the periapse and in/outbound segments on the orbit were utilized, when the spacecraft is between 140 and 1,000 km from the planet's surface. The former refers to measurements made near the periapse with scans oriented perpendicular to the spacecraft motion. The latter refers to the two orbit segments when the spacecraft is well outside the atmosphere, just before and just after the periapse segment, to ensure at least one daylight segment with a similar scanning motion. In the limb scanning mode, the relative size of a pixel on the tangent point is larger than at the periapse, due to the increased distance from Mars; nevertheless, reliable retrievals are readily extracted from these data.

When MAVEN is moving through its periapse orbital segment, IUVS uses a scan mirror to scan across the limb and create vertical profiles of emitted atmospheric radiation over the altitude range of 60–250 km. IUVS takes up to 12 periapse limb scans of each orbit in a ~22 min observation time period spanning ~45° across Mars and 6 in/outbound limb scans between 25° and 100° around the planet depending on the tangent point's orientation to the surface. To facilitate MAVEN's extended mission, in April 2019, the spacecraft periapse was raised between 180 and 230 km and the orbit shortened to ~4 hr, where we now take 14 scans rather than 12. Together, these data sets constitute almost continuous monitoring of the Martian atmosphere from 2015 to 2022, although only dayside data are utilized as solar fluorescent scattering is necessary to observe Mg⁺ with IUVS (Schneider, Deighan, Stewart, et al., 2015).

2.2. Data Processing

The MgII doublet emission observed herein is caused by resonant fluorescent solar scattering of UV photons at 280 nm as opposed to direct excitation emission during ablation. To model the spectrum of these metallic species, its line positions, the atomic constants for resonant scattering, and the solar Mid-UV spectrum (Dymond et al., 2003; Kelleher & Podobedova, 2008; Smith et al., 1995) were utilized. Multiple linear regression fits of independent spectral components are able to extract the MgII doublet brightness from a composite spectrum fit of emission of ambient atmospheric gases (CO, CO₂⁺, N₂, etc.) and were subsequently co-added (M. M. J. Crismani et al., 2018; Stevens et al., 2015). Data processing techniques for these UV spectra have been previously outlined in greater detail in other MAVEN/IUVS papers (Evans et al., 2015; M. M. J. Crismani et al., 2017, 2018; Jain et al., 2015; Schneider, Deighan, Jain, et al., 2015; Stevens et al., 2015).

When Mg⁺ densities are small enough (<2,500 cm⁻³) such that they can be considered optically thin at the line center rather than using a forward model retrieval (M. M. J. Crismani et al., 2018); the Mg⁺ concentration can be retrieved using a simple Abel transform (Chamberlain & Hunten, 1990), which requires single scattering with no absorption. Reported retrieved density uncertainties are calculated through traditional error propagation of the IUVS instrument random and estimated uncertainties. Systematic retrieved density uncertainties are a combination of uncertainties in the parameters (scale height and atomic g-factors) as well as the IUVS MUV calibration uncertainties, estimated to be ±30%. All of the data described herein are considered optically thin as the peak densities observed do not greatly exceed 500 cm⁻³. This discussion has been previously covered in greater detail in (M. M. J. Crismani et al., 2017, 2018).

This work benefits from many years of observation of Mg⁺ abundance, and two new post-retrieval data analysis filters were implemented to create statistically useful averages and medians. First, as MgII emission is due to resonant scattering of solar photons, this necessarily requires that the location of the tangent point of any observation considered in an average or median should be in “daylight.” At the surface this concept is simple, where the solar photons are extinguished at SZAs larger than 90°. However, at any altitude above the surface solar photons may illuminate tangent points past 90° SZA. The formula for the maximum illuminated SZA (θ_{\max}) for given tangent point at an altitude (A) is:

$$\theta_{\max} = 90^\circ + \arccos\left(\frac{R_{\text{Mars}}}{R_{\text{Mars}} + A}\right)$$

where R_{Mars} is the mean radius of Mars, 3,390 km. Moreover, this filter serves to caution the reader that observations of nightside Mg⁺ with IUVS are impossible and would require a separate study from the MAVEN/NGIMS instrument (Mahaffy et al., 2015); however, these data only sample the topside of the meteoric metal profiles (above 140 km) and are not representative of the peak abundances or meteoric influxes.

The second important caveat to note when interpreting Mg⁺ retrievals is that at altitudes below 60 km, the scattered solar continuum dominates the IUVS detector signal. While the source of this scattered continuum is likely

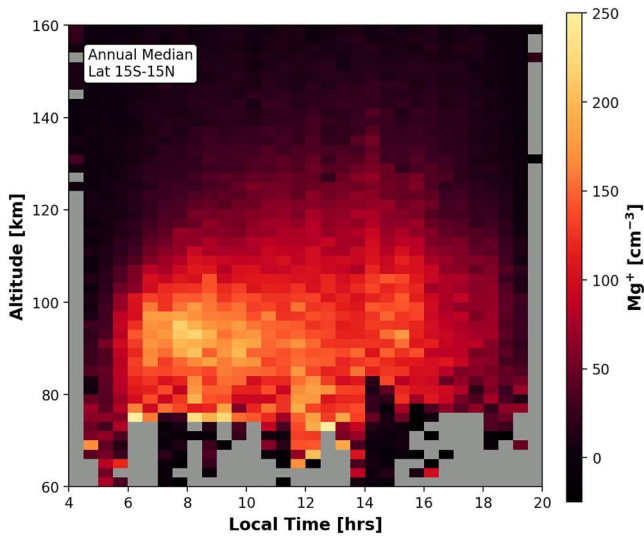


Figure 1. The median Mg^+ concentration (atoms per cubic centimeter) at equatorial latitudes, over the mission to date (MY 32–36), plotted against altitude vertically and local time horizontally. A notable enhancement in Mg^+ concentration appears in the dawn hours. This enhancement disappears at higher latitudes (see Figure S1 in Supporting Information S1), where the diurnal forcing is weaker. The dark gray color represents locations where insufficient data exist, here and in all subsequent figures.

to be aerosols in the lower atmosphere, the precise modeling of this feature is hampered by an apparent change in the spectral shape from high altitudes (above 150 km) to the lowest altitudes (60 km). Significant testing of appropriate continuum shapes has been undertaken; however, for the purposes of this work, it is important to note that when the strength of the scattered continuum is too great, any difference between the spectral fit and data will inevitably lead to erroneous retrievals. Characterization of the reliability of this difference was undertaken for this work and a practical limit was set when the solar signal exceeded brightnesses of 500 kR for periapse data and 100 kR for limb data.

Extremely large and/or negative values exist after the retrieval process, which are not due to reliable fits, as seen in residual fit shapes, but instead may be caused by non-atmospheric instrumental effects. These include, but are not limited to, cosmic ray impacts on the detector, background stars falling in the optical path, improper temperature-dependent wavelength alignment, or any other combination of other random errors. To restrict the small fraction (<2%) of these outlying values from disproportionately affecting any results presented herein, binned medians are presented here rather than averages, where bin sizes were constructed to never permit a median of less than 10 observations in any subdivided geophysical grouping. While individual observation uncertainties are of the order 30%, the binned observations have a minimum number of observations of 10, which reduces this random uncertainty by the square root of 10 at the least. Therefore, the variations we see here, which are larger than 10%, are not expected to be due to orbit to orbit variation or instrument performance.

3. Results

With these constraints implemented in the data processing pipeline, this work draws on seven Earth years of data, from Martian Year (MY) 32–36, spanning all Solar Longitudes (L_S), latitudes, and geographic longitudes. The results presented herein constitute the most comprehensive view of Mg^+ at Mars, binned in several ways, comparing altitude, local times, L_S , latitude, and longitude. Note that the present paper does not investigate any interannual variability at the cost of completeness in these primary binning variables. Moreover, this work necessarily ignores the orbit to orbit variability and the drivers of that variability (meteor showers, ionospheric interactions with B-fields, etc.). Initial analysis searching for meteor shower correlations found these to be below the first-order effects described herein; therefore, these results are presented to permit any secondary effects, if observable, to be investigated in a subsequent manuscript.

3.1. Equatorial Dawnside Enhancement

Figure 1 presents the grand composite view of equatorial ($15^\circ\text{S} < \text{lat} < 15^\circ\text{N}$) Mg^+ as a function of local time over the eight Earth years (2014–2022) observation period. There exists a strong apparent dayside variation where peak values at 0800 hr exceed 200 cm^{-3} compared to those at 1,600 hr that are closer to 100 cm^{-3} . The dawn-side maximum in Mg^+ concentration cannot be due to photo-ionization as this would cause a peak around midday or later. A potential explanation is the vertical transport of Mg^+ ; the mixing ratio of Mg^+ increases by a factor of ~ 5 between 95 and 105 km (J. M. C. Plane et al., 2018), so downward transport of air from above 95 km during the night would explain the 2–3 fold increase in Mg^+ number density at 95 km (Withers et al., 2011).

The previously published 1D model (Plane et al., 2018) showed that the Mg^+ ion mixing ratio increases above 90 km, in agreement with IUVS measurements at low- and mid-latitudes. Therefore, downward transport of air from aloft will increase the Mg^+ concentration around 90 km, as observed. The evidence for tidal descent comes from the temperature, which shows a marked increase between 0400 and 0800 hrs in this region, consistent with adiabatic heating of the descending air. Since ion-molecule chemistry is not strongly temperature-dependent, the change in reaction rates is a secondary effect: at higher temperatures, the rate at which Mg^+ forms clusters with CO_2 is reduced, which then reduces the rate of conversion to Mg via dissociative recombination with electrons. Therefore, the main tidal effect is to bring air with a higher Mg^+ mixing ratio downwards. Dayside heating in the

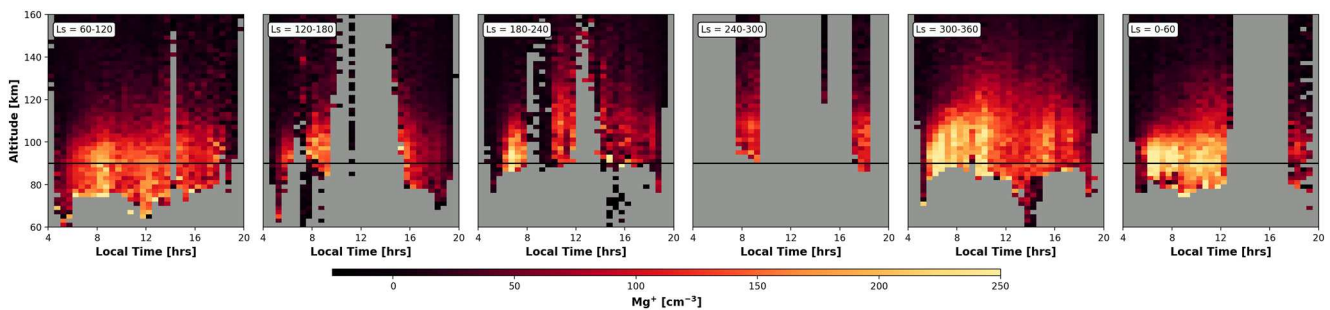


Figure 2. The median dayside atmospheric Martian Mg^+ (ions per cubic centimeter) for eight Earth years (2014–2022) is presented for six segmented “seasons” of the Martian Year (see text) beginning at $L_s = 60^\circ\text{--}120^\circ$ (near aphelion) with an altitude (km) shown vertically and local time (hr) horizontally, with an altitude reference at 90 km (black line). These data include all local times where Mg^+ is illuminated by the Sun.

mesosphere and thermosphere has been observed over the MY, with heating in the afternoon and cooling toward the dawn and dusk terminator (Jain et al., 2021). Future 3D-GCM efforts will focus on comparing the Mg^+ concentrations with the observed temperatures and model results.

3.2. Seasonal Shifts in Peak Ablation Altitude

Figure 2 presents the median dayside equatorial ($15^\circ\text{S} < \text{lat} < 15^\circ\text{N}$) atmospheric Martian Mg^+ (cm^{-3}) for all observations, where six “seasons” of the MY were delineated. Each of these “seasons” has a length of $60^\circ L_s$, where summer and winter solstices are centered around their own seasons, but the two equinoxes occur in the middle of the four pseudo-seasons, such as the end of Southern Early Spring ($L_s = 120^\circ\text{--}180^\circ$) and Southern Late Spring ($L_s = 180^\circ\text{--}240^\circ$). The framing of the seasons around the dynamical state of the atmosphere is utilized herein to link Mg^+ abundances and peak altitudes with the larger atmospheric circulation patterns.

The leftmost panel of Figure 2 begins at $L_s = 60^\circ$ (Southern Winter). The peak concentration of Mg^+ appears at altitudes of 80–90 km when Laboratoire de Météorologie Dynamique-GCM (Millour et al., 2015) global mean temperatures demonstrate lower average atmospheric temperatures during aphelion. Moving left to right until panel d (Southern Summer), peak Mg^+ appears at altitudes of 95–105 km, when modeled average temperatures increase to their highest during perihelion due to increased insolation. IUVS observations are obtained with respect to altitude; however, mesospheric pressures have been observed to vary with season (Jain et al., 2015; Jakosky et al., 2017; Slipski et al., 2018). Ablation of interplanetary dust particles is dependent on ambient pressure and temperature, with atmospheric chemistry controlling the top and bottom scale heights of the layer as well as the peak altitude as observed by IUVS. For example, cooling of the temperature vertical structure shifts the minimum atmospheric density (or pressure) level necessary to start thermal ablation to lower altitudes (Carrillo-Sánchez et al., 2015, 2020). However, the pressure level at which each meteoric metal is released is constant, where alkali elements—such as Na and K—are always released at 0.01 Pa, in contrast to the main metals—Mg, Si, and Fe—which are ablated when pressures exceed 0.1 Pa (Bones et al., 2016). The magnitude of the observed peak concentration of Mg^+ is consistent throughout the year even with the diurnal enhancement on the dawn side as discussed in Section 3.1.

3.3. Latitudinal Distribution of Mg^+

A hemispheric view of dayside Mg^+ with season (Figure 3), where altitudes (vertically) and latitude (horizontally) are presented for median solar illuminated (5–20 hr) Mg^+ concentrations to highlight the use of meteoric ions as a tracer of mesospheric dynamics. This subset of seasons (for the remainder see Figure S1 in Supporting Information S1) show three unique sets of behaviors, potentially corresponding to global motions of the atmosphere.

During the southern late autumn (Figure 3a), the peak altitude of Mg^+ concentration appears to slightly rise from the southern pole to the equator to northern latitudes, with the topside of the layer extending higher at equatorial latitudes than either the midlatitude or polar region. At equatorial latitudes, the scale heights of Mg^+ are much shallower (Mg^+ is more vertically extended) than near mid-northern or mid-southern latitudes, which may indicate that vertical mixing through eddy diffusion is rapid. This result is not surprising as these Mg^+ ions are long lived (timescale of hours to days) and in contrast to ambient ions (e.g., O_2^+ , timescales of minutes) are not

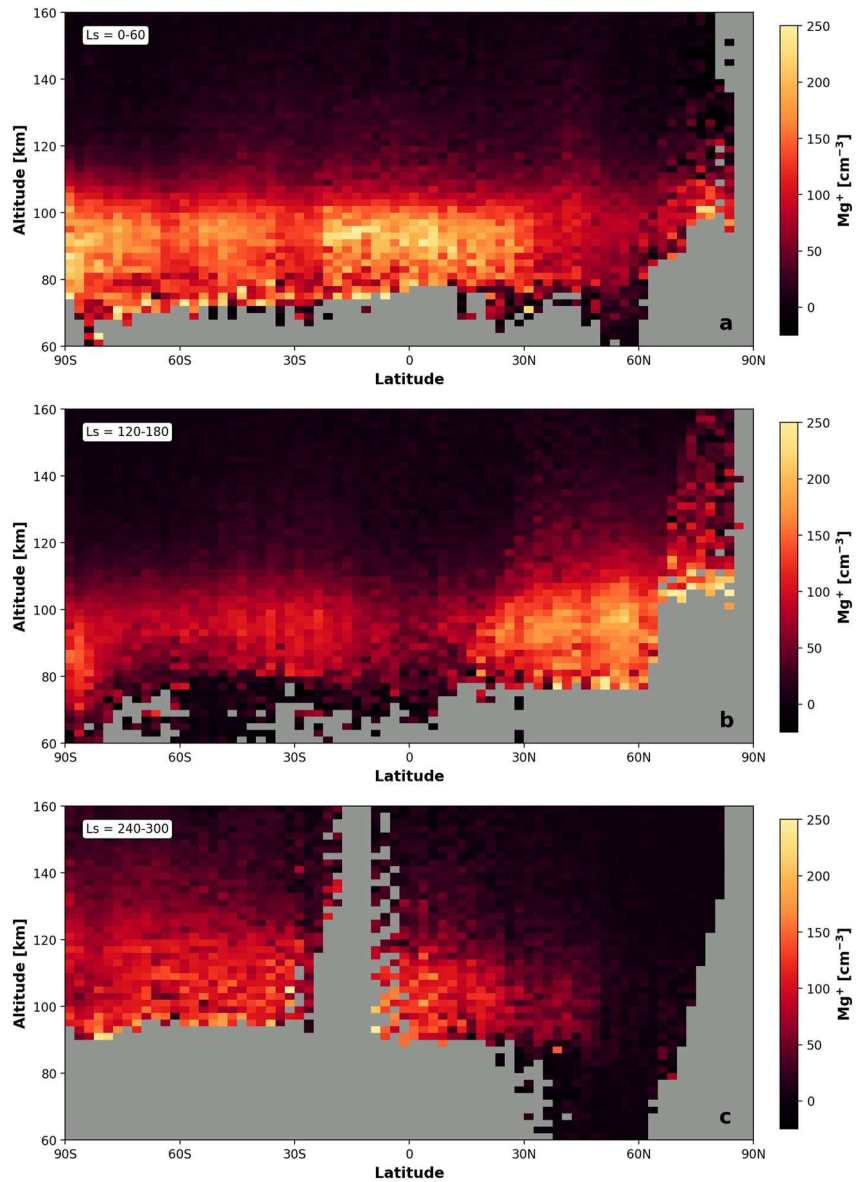


Figure 3. Median Mg⁺ concentration (ions cm⁻³) as a function of altitude (vertically) and latitude (horizontally), where data collected over Mars Atmosphere and Volatile Evolution's mission is sorted by season. (a) $L_S = 0^\circ\text{--}60^\circ$: notable features include a rising peak altitude and an extended topside layer toward equatorial latitudes. (b) $L_S = 120^\circ\text{--}180^\circ$: a decrease in Mg⁺ near equatorial latitudes and a dichotomy between the hemispheres, with larger peak values of Mg⁺ at midlatitudes appearing in the North. (c) $L_S = 240^\circ\text{--}300^\circ$: a much higher abundance of Mg⁺ in the southern than the northern hemisphere.

produced in situ (Plane et al., 2018); therefore, the former traces the dynamics of the atmosphere and the latter shows the sources of ionization and resultant chemistry.

During the southern late spring (Figure 3b), the peak altitude of Mg⁺ at the south pole sinks to as low as 80 km, with a topside that extends to 100 km. While midlatitude abundances of Mg⁺ peak near 95–100 km, there is a noticeable decrease in Mg⁺ near equatorial latitudes. There is a marked dichotomy in the overall peak Mg⁺ abundance where there is more Mg⁺ in northern than southern hemispheres, seen also in Figure S1 in Supporting Information S1. Whether this is due to the meteor input distribution, dynamics, or meteoric chemistry should be investigated with subsequent modeling efforts that include each of these relevant drivers.

The most unexpected observation contained herein is the relative disappearance of Mg⁺ during southern summer (Figure 3c) despite good observational coverage in this period. During this period Mg⁺ at all latitudes becomes

reduced compared to any other season of the MY (see Figure S2 in Supporting Information S1). Mg^+ is more vertically extended at southern latitudes with larger values at each altitude ($\sim 120 \text{ cm}^{-3}$ at 120 km) compared to other seasons; however, these values are lower than typical peak values ($\sim 250 \text{ cm}^{-3}$ at 100 km), with little to no Mg^+ present in northern latitudes (above 40°N). While the total number of observations during this season is not as well spread in local time as other seasons, comparisons within a single bracket of local times serve to confirm this result as we see consistent values (high or low) across latitudes in other seasons. Whereas during this season, the Mg^+ appears to disappear at all local times and most altitudes moving toward high northern latitudes. Since this is southern summer, it should be noted that this is also potentially the dustiest time period of the MY (Montabone et al., 2020). While dust in the lower atmosphere has been linked to the propagation of water vapor in the mesosphere and as the lower atmosphere heats dramatically compared to non-dust storm years (A. A. Fedorova et al., 2020; A. Fedorova et al., 2018; Aoki et al., 2019; Chaffin et al., 2017, 2021; Chaufray et al., 2019; Guzewich et al., 2019; Kass et al., 2016; Neary et al., 2019; Streeter et al., 2020; Villanueva et al., 2021), there is no obvious explanation for what process dust in the lower atmosphere could remove Mg^+ in the upper atmosphere.

3.4. Geographic Variations in Mg^+ and Absence of B-Field Influence

Solar thermal heating produces global atmospheric tides, longitudinal variations in temperature, density, and pressure whose periodicity are fractions of the Martian day (England et al., 2016; Forbes et al., 2020; Hanel et al., 1972; Lo et al., 2015; Schneider et al., 2020). These tides serve to redistribute energy throughout the atmosphere, both horizontally and through the vertical propagation of these tides. Tidal waves can be either migrating or non-migrating, where the former refers to sun-synchronous waves and the latter refers to waves that move either east or west relative to the apparent motion of the sun (including stationary relative to the surface). These tidal waves are denoted by their temporal harmonic, propagation direction, and wave number; for example, a diurnally propagating westward wave with wave number 3 would be called DW3.

Figure 4 presents geographic variations in Mg^+ during $L_S = 60^\circ\text{--}120^\circ$, where dayside medians and their differences show enhancements and reductions of Mg^+ , whose origin is likely tidal. Averaging all of the dayside hours will tend to eliminate semi-diurnal variations and enhance either stationary or diurnal variations, so the tidal variation seen in Figure 4 is likely DE2 (diurnal, eastward); however, further investigation will be necessary to determine the motion in longitude with local time. These variations are also seen in a previous season ($L_S = 0^\circ\text{--}60^\circ$) although they were there confined to equatorial latitudes (Figure S3 in Supporting Information S1). Previous observations with the Mars Climate Sounder and GCM modeling showed similar DE2 wave patterns between 76 and 108 km present between $L_S = 0^\circ\text{--}120^\circ$ (Forbes et al., 2020), consistent with the observations presented here, and weakened throughout the remainder of the MY. Tidal variations were observed in a similar season with MAVEN/IUVS using observations of Nitric Oxide nightglow; however, these emissions occur at much lower altitudes, and it is perhaps not unexpected that the locations of these enhancements do not line up at the same longitudinal regions (Schneider et al., 2020).

The variations here do not indicate novel meteoric chemistry nor do we anticipate that depletions are the result of an enhanced chemical sink process. Instead, the total number of meteoric species is roughly constant, which can appear enhanced by compressing the entire layer in altitude or reducing the rate at which Mg^+ is converted into other species by affecting chemistry in the bottom side of the Mg^+ layer. However, these statements will require further validation in cross comparisons with a fully 3D-GCM that includes meteoric metal chemistry.

Latitude and longitude maps of Mg^+ abundance at a given altitude (Figure 4, Figure S3 in Supporting Information S1) can be compared to maps of global remnant crustal magnetization (Connerney et al., 2001), which are oriented strongly E-W between 30° to 90°S latitude and $150^\circ\text{--}240^\circ$ longitude, and there does not appear to be any correlation (positive or negative). If the dynamics or chemistry of Mg^+ were strongly influenced by crustal magnetization direction or magnitude, one would expect horizontal layers of enhanced and depleted Mg^+ emission near these field regions, and yet there is no preference in comparison to similar latitudes in the northern hemisphere, even within the same “season.” This is in contrast to discrete auroral emissions that are directly influenced by remnant crustal magnetization (Bertaux et al., 2005; Schneider et al., 2018).

4. Conclusions

Prior to the Martian insertion of the MAVEN spacecraft in 2014, ionospheric observations of a transient M_3 or M_m layer of electrons near 90 km, coincident with modeled ablation heights (Pätzold et al., 2005; Withers

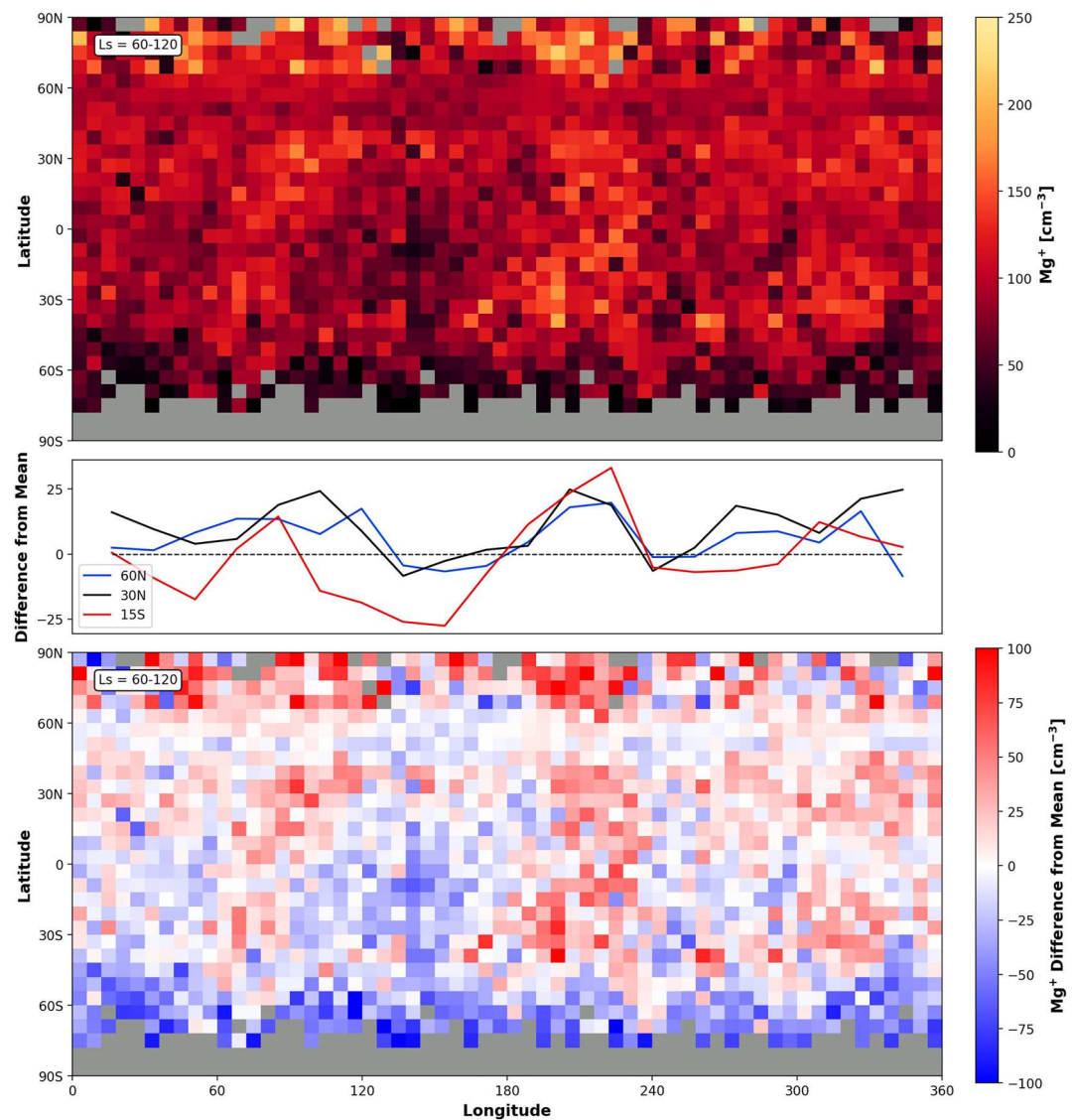


Figure 4. The top panel presents the median Mg⁺ between 80 and 110 km against latitude and longitude for the season $L_s = 60^\circ\text{--}120^\circ$ (Southern Winter). The bottom panel shows the difference of each point from the mean value of the entire map, and the middle panel is a cross section of this map at the latitudes highlighted in the legend.

et al., 2008), were presented as evidence of intermittent meteoric ablation. However, after the meteor shower of comet Siding Spring (M. M. J. Crismani et al., 2018; Schneider, Deighan, Stewart, et al., 2015) and discovery of a persistent layer of meteoric ions (M. M. J. Crismani et al., 2017) provided the first observations of atomic and ionic metal species it was possible to determine that the origin of these features in the radio occultation observations was not meteoric (M. M. J. Crismani et al., 2019). Initial monitoring of the Mg⁺ layer due to sporadic meteoroids indicated that it was a persistent layer with a fixed altitude and abundance (M. M. J. Crismani et al., 2017). However, such an early and simplified view has been supplanted by the wealth of data accumulated since 2015.

The Mg⁺ layer seems to be dynamic, with peak ablation altitudes shifting, abundances fluctuating, and variations in the slope of the top and bottom-sides of the Mg⁺ layer, all likely directly related to the underlying atmospheric structure and meteoric chemistry. At the equator, a multi-year analysis shows an enhancement of Mg⁺ at morning local times whose layer topside increases throughout the day. Separating these observations by season, the peak altitude Mg⁺ appears to respond to the background atmosphere as the former shifts up and down in altitude. Using zonal medians to compare across latitudes, the Mg⁺ layer peak altitude can dip as low as 80 km near the south pole and as high as 105 km at equatorial/mid-latitudes. Overall abundances also vary dramatically, in excess

of the average 250 ions cm^{-3} reported in (M. M. J. Crismani et al., 2017) to averages of 300–500 ions cm^{-3} in some cases, but the reduction of Mg^+ in specific seasons warrants further investigation. Finally, in two seasons ($L_s = 0^\circ\text{--}120^\circ$), the geographic distribution may be linked to tidal variations in the background atmosphere.

This data set represents nearly continuous monitoring of the Mg^+ layer in a variety of geophysical conditions, and the results found herein will provide important constraints for the next generation of meteoric ion chemistry and atmospheric circulation modeling at Mars. Model-observation comparisons should provide insights into mesospheric transport, chemistry and interplanetary dust particle sources. Previous discrepancies between model predictions and metal ion observations led to the development of a novel nucleation scheme for mesospheric clouds (Plane et al., 2018), and we expect this data set to provide the impetus to future advances in atmospheric chemistry. Overall, this represents the broadest investigation of meteoric metal ions, summarizes their first-order behavior, and outlines new model challenges for the future.

Conflict of Interest

The authors declare no conflicts of interest relevant to this study.

Data Availability Statement

The level 1B data used herein are calibrated level data (Deighan, 2018), publicly available on the Atmospheres node of the NASA Planetary Data System tagged “periapse” (https://pds-atmospheres.nmsu.edu/data_and_services/atmospheres_data/MAVEN/limb.html). The filtered data set is hosted on Zenodo and is publicly available (M. Crismani, 2022).

Acknowledgments

The authors would like to thank Scott England and Aishwarya Kumar for fruitful discussions on waves and tides. MC was supported in part by the NASA Award 80NSSC21M0110 through the NASA Goddard Space Flight Center. NASA supports the MAVEN mission through the Mars Scout program. DJ and JDCS were supported through the NASA ISFM Program. JMCP and WF were supported by the European Research Council (Project 291332-CODITA) and UK Science and Technology Facilities Council (Project ST/T000279/1).

References

- Aoki, S., Vandaele, A. C., Daerden, F., Villanueva, G. L., Liuzzi, G., Thomas, I. R., et al. (2019). Water vapor vertical profiles on Mars in dust storms observed by TGO/NOMAD. *Journal of Geophysical Research: Planets*, 124(12), 3482–3497. <https://doi.org/10.1029/2019JE006109>
- Benna, M., Mahaffy, P. R., Grebowsky, J. M., Plane, J. M. C., Yelle, R. V., & Jakosky, B. M. (2015). Metallic ions in the upper atmosphere of Mars from the passage of comet C/2013 A1 (Siding Spring). *Geophysical Research Letters*, 42(12), 4670–4675. <https://doi.org/10.1002/2015GL064159>
- Bertaux, J.-L., Leblanc, F., Witasse, O., Quemerais, E., Liliensten, J., Stern, S. A., et al. (2005). Discovery of an aurora on Mars. *Nature*, 435(7043), 790–794. <https://doi.org/10.1038/nature03603>
- Bones, D. L., Gómez Martín, J. C., Empson, C. J., Carrillo Sánchez, J. D., James, A. D., Conroy, T. P., & Plane, J. M. C. (2016). A novel instrument to measure differential ablation of meteorite samples and proxies: The Meteoric Ablation Simulator (MASI). *Review of Scientific Instruments*, 87(9), 094504. <https://doi.org/10.1063/1.4962751>
- Carrillo-Sánchez, J. D., Gómez-Martin, J. C., Bones, D. L., Nesvorný, D., Pokorný, P., Benna, M., et al. (2020). Cosmic dust fluxes in the atmospheres of Earth, Mars, and Venus. *Icarus*, 335, 113395. <https://doi.org/10.1016/j.icarus.2019.113395>
- Carrillo-Sánchez, J. D., Plane, J. M. C., Feng, W., Nesvorný, D., & Janches, A., et al. (2015). On the size and velocity distribution of cosmic dust particles entering the atmosphere. *Geophysical Research Letters*, 42(15), 6518–6525. <https://doi.org/10.1002/2015GL065149>
- Chaffin, M. S., Deighan, J., Schneider, N. M., & Stewart, A. I. F. (2017). Elevated atmospheric escape of atomic hydrogen from Mars induced by high-altitude water. *Nature Geoscience*, 10(3), 174–178. <https://doi.org/10.1038/ngeo2887>
- Chaffin, M. S., Kass, D. M., Aoki, S., Fedorova, A. A., Deighan, J., Connour, K., et al. (2021). Martian water loss to space enhanced by regional dust storms. *Nature Astronomy*, 5(10), 1036–1042. <https://doi.org/10.1038/s41550-021-01425-w>
- Chamberlain, J., & Hunten, D. (1990). *Theory of planetary atmospheres: An introduction to their physics and chemistry*. Academic Press.
- Chaufray, J.-Y., Chaffin, M., Deighan, J., Jain, S., Schneider, N., Mayyasi, M., & Jakosky, B. (2019). Effect of the 2018 Martian global dust storm on the CO_2 density in the lower nightside thermosphere observed from MAVEN/IUVS Lyman-alpha absorption. *Geophysical Research Letters*, 47(ja), e2019GL082889. <https://doi.org/10.1029/2019GL082889>
- Connerney, J. E. P., Acuña, M. H., Wasilewski, P. J., Kletetschka, G., Ness, N. F., Rème, H., et al. (2001). The global magnetic field of Mars and implications for crustal evolution. *Geophysical Research Letters*, 28(21), 4015–4018. <https://doi.org/10.1029/2001GL013619>
- Connour, K., Schneider, N. M., Milby, Z., Forget, F., Alhosani, M., Spiga, A., et al. (2020). Mars's twilight cloud band: A new cloud feature seen during the Mars year 34 global dust storm. *Geophysical Research Letters*, 47(1), e2019GL084997. <https://doi.org/10.1029/2019GL084997>
- Crismani, M. (2022). Mg^+ concentrations from IUVS limb scans [Dataset]. Zenodo. <https://doi.org/10.5281/ZENODO.7415974>
- Crismani, M. M. J., Deighan, J., Schneider, N. M., Plane, J. M. C., Withers, P., Halekas, J., et al. (2019). Localized ionization hypothesis for transient ionospheric layers. *Journal of Geophysical Research: Space Physics*, 124(6), 4870–4880. <https://doi.org/10.1029/2018JA026251>
- Crismani, M. M. J., Schneider, N. M., Evans, J. S., Plane, J. M. C., Carrillo-Sánchez, J. D., Jain, S., et al. (2018). The impact of comet Siding Spring's meteors on the Martian atmosphere and ionosphere. *Journal of Geophysical Research: Planets*, 123(10), 2613–2627. <https://doi.org/10.1029/2018JE005750>
- Crismani, M. M. J., Schneider, N. M., Plane, J. M. C., Evans, J. S., Jain, S. K., Chaffin, M. S., et al. (2017). Detection of a persistent meteoric metal layer in the Martian atmosphere. *Nature Geoscience*, 10(6), 401–404. <https://doi.org/10.1038/ngeo2958>
- Deighan, J. (2018). *Mars Atmosphere and Volatile Evolution (MAVEN) Imaging Ultraviolet Spectrograph (IUVS) calibrated-level data product bundle*. NASA Planetary Data System. <https://doi.org/10.17189/1518946>
- Deighan, J., Jain, S. K., Chaffin, M. S., Fang, X., Halekas, J. S., Clarke, J. T., et al. (2018). Discovery of a proton aurora at Mars. *Nature Astronomy*, 2(10), 802–807. <https://doi.org/10.1038/s41550-018-0538-5>

- Dymond, K. F., Wolfram, K. D., Budzien, S. A., Nicholas, A. C., McCoy, R. P., & Thomas, R. J. (2003). Middle ultraviolet emission from ionized iron. *Geophysical Research Letters*, *30*(1), 3-1-3-4. <https://doi.org/10.1029/2002GL015060>
- England, S. L., Liu, G., Withers, P., Yiğit, E., Lo, D., Jain, S., et al. (2016). Simultaneous observations of atmospheric tides from combined in situ and remote observations at Mars from the MAVEN spacecraft. *Journal of Geophysical Research: Planets*, *121*(4), 594–607. <https://doi.org/10.1002/2016JE004997>
- Evans, J. S., Stevens, M. H., Lumpe, J. D., Schneider, N. M., Stewart, A. I. F., Deighan, J., et al. (2015). Retrieval of CO₂ and N₂ in the Martian thermosphere using dayglow observations by IUVS on MAVEN. *Geophysical Research Letters*, *42*(21), 9040–9049. <https://doi.org/10.1002/2015GL065489>
- Fedorova, A., Bertaux, J.-L., Betsis, D., Montmessin, F., Korablev, O., Maltagliati, L., & Clarke, J. (2018). Water vapor in the middle atmosphere of Mars during the 2007 global dust storm. *Icarus*, *300*, 440–457. <https://doi.org/10.1016/j.icarus.2017.09.025>
- Fedorova, A. A., Montmessin, F., Korablev, O., Luginin, M., Trokhimovskiy, A., Belyaev, D. A., et al. (2020). Stormy water on Mars: The distribution and saturation of atmospheric water during the dusty season. *Science*, *367*(6475), 297–300. <https://doi.org/10.1126/science.aay9522>
- Feng, W., Marsh, D. R., Chipperfield, M. P., Janches, D., Höffner, J., Yi, F., & Plane, J. M. C. (2013). A global atmospheric model of meteoric iron. *Journal of Geophysical Research: Atmospheres*, *118*(16), 9456–9474. <https://doi.org/10.1002/jgrd.50708>
- Forbes, J. M., Zhang, X., Forget, F., Millour, E., & Kleinböhl, A. (2020). Solar tides in the middle and upper atmosphere of Mars. *Journal of Geophysical Research: Space Physics*, *125*(9), e2020JA028140. <https://doi.org/10.1029/2020JA028140>
- Grebowsky, J. M., Benna, M., Plane, J. M. C., Collinson, G. A., Mahaffy, P. R., & Jakosky, B. M. (2017). Unique, non-Earthlike, meteoritic ion behavior in upper atmosphere of Mars. *Geophysical Research Letters*, *44*(7), 3066–3072. <https://doi.org/10.1002/2017GL072635>
- Guzewich, S. D., Lemmon, M., Smith, C. L., Martínez, G., de Vicente-Retortillo, Á., Newman, C. E., et al. (2019). Mars Science Laboratory Observations of the 2018/Mars year 34 global dust storm. *Geophysical Research Letters*, *46*(1), 71–79. <https://doi.org/10.1029/2018GL080839>
- Hanel, R., Conrath, B., Hovis, W., Kunde, V., Lowman, P., Maguire, W., et al. (1972). Investigation of the Martian environment by infrared spectroscopy on Mariner 9. *Icarus*, *17*(2), 423–442. [https://doi.org/10.1016/0019-1035\(72\)90009-7](https://doi.org/10.1016/0019-1035(72)90009-7)
- Hartwick, V. L., Toon, O. B., & Heavens, N. G. (2019). High-altitude water ice cloud formation on Mars controlled by interplanetary dust particles. *Nature Geoscience*, *12*(7), 516–521. <https://doi.org/10.1038/s41561-019-0379-6>
- Jain, S. K., Soto, E., Evans, J. S., Deighan, J., Schneider, N. M., & Bougher, S. W. (2021). Thermal structure of Mars' middle and upper atmospheres: Understanding the impacts of dynamics and solar forcing. *Icarus*, 114703. <https://doi.org/10.1016/j.icarus.2021.114703>
- Jain, S. K., Stewart, A. I. F., Schneider, N. M., Deighan, J., Stiepen, A., Evans, J. S., et al. (2015). The structure and variability of Mars upper atmosphere as seen in MAVEN/IUVS dayglow observations. *Geophysical Research Letters*, *42*(21), 9023–9030. [https://doi.org/10.1002/2015GL065419@10.1002/\(ISSN\)1944-8007.MAVEN1](https://doi.org/10.1002/2015GL065419@10.1002/(ISSN)1944-8007.MAVEN1)
- Jakosky, B. M., Brain, D., Chaffin, M., Curry, S., Deighan, J., Grebowsky, J., et al. (2018). Loss of the Martian atmosphere to space: Present-day loss rates determined from MAVEN observations and integrated loss through time. *Icarus*, *315*, 146–157. <https://doi.org/10.1016/j.icarus.2018.05.030>
- Jakosky, B. M., Grebowsky, J. M., Luhmann, J. G., Connerney, J., Eparvier, F., Ergun, R., et al. (2015). MAVEN observations of the response of Mars to an interplanetary coronal mass ejection. *Science*, *350*(6261), aad0210. <https://doi.org/10.1126/science.aad0210>
- Jakosky, B. M., Slipski, M., Benna, M., Mahaffy, P., Elrod, M., Yelle, R., et al. (2017). Mars' atmospheric history derived from upper-atmosphere measurements of ³⁸Ar/²⁶Ar. *Science*, *355*(6332), 1408–1410. <https://doi.org/10.1126/science.aai7721>
- Janches, D., Bruzzone, J. S., Pokorný, P., Carrillo-Sánchez, J. D., & Sarantos, M. (2020). A comparative modeling study of the seasonal, temporal, and spatial distribution of meteoroids in the upper atmospheres of Venus, Earth, and Mars. *The Planetary Science Journal*, *1*(3), 59. <https://doi.org/10.3847/PSJ/abba35>
- Jiang, F. Y., Yelle, R. V., Jain, S. K., Cui, J., Montmessin, F., Schneider, N. M., et al. (2019). Detection of mesospheric CO₂ ice clouds on Mars in southern summer. *Geophysical Research Letters*, *46*(14), 7962–7971. <https://doi.org/10.1029/2019GL082029>
- Kass, D. M., Kleinböhl, A., McCleese, D. J., Schofield, J. T., & Smith, M. D. (2016). Interannual similarity in the Martian atmosphere during the dust storm season. *Geophysical Research Letters*, *43*(12), 6111–6118. <https://doi.org/10.1002/2016GL068978>
- Kelleher, D. E., & Podobedova, L. I. (2008). Atomic transition probabilities of sodium and magnesium. A critical compilation. *Journal of Physical and Chemical Reference Data*, *37*(1), 267–706. <https://doi.org/10.1063/1.2735328>
- Langowski, M. P., von Savigny, C., Burrows, J. P., Feng, W., Plane, J. M. C., Marsh, D. R., et al. (2015). Global investigation of the Mg atom and ion layers using SCIAMACHY/Envisat observations between 70 and 150 km altitude and WACCM-Mg model results. *Atmospheric Chemistry and Physics*, *15*(1), 273–295. <https://doi.org/10.5194/acp-15-273-2015>
- Lo, D. Y., Yelle, R. V., Schneider, N. M., Jain, S. K., Stewart, A. I. F., England, S. L., et al. (2015). Nonmigrating tides in the Martian atmosphere as observed by MAVEN IUVS. *Geophysical Research Letters*, *42*(21), 9057–9063. [https://doi.org/10.1002/2015GL066268@10.1002/\(ISSN\)1944-8007.MAVEN1](https://doi.org/10.1002/2015GL066268@10.1002/(ISSN)1944-8007.MAVEN1)
- Mahaffy, P. R., Benna, M., Elrod, M., Yelle, R. V., Bougher, S. W., Stone, S. W., & Jakosky, B. M. (2015). Structure and composition of the neutral upper atmosphere of Mars from the MAVEN NGIMS investigation. *Geophysical Research Letters*, *42*(21), 8951–8957. <https://doi.org/10.1002/2015GL065329>
- Martín, J. C. G., Bones, D. L., Carrillo-Sánchez, J. D., James, A. D., Trigo-Rodríguez, J. M., Jr, B. F., & Plane, J. M. C. (2017). Novel experimental simulations of the atmospheric injection of meteoric metals. *The Astrophysical Journal*, *836*(2), 212. <https://doi.org/10.3847/1538-4357/aa5c8f>
- McClintock, W. E., Schneider, N. M., Holsclaw, G. M., Clarke, J. T., Hoskins, A. C., Stewart, I., et al. (2015). The Imaging Ultraviolet Spectrograph (IUVS) for the MAVEN mission. *Space Science Reviews*, *195*(1), 75–124. <https://doi.org/10.1007/s11214-014-0098-7>
- Millour, E., Forget, F., Spiga, A., & Navarro, T. (2015). *The Mars climate database (MCD version 5.2)* (Vol. 10). European Planetary Science Congress.
- Montabone, L., Spiga, A., Kass, D. M., Kleinböhl, A., Forget, F., & Millour, E. (2020). Martian year 34 column dust climatology from Mars climate sounder observations: Reconstructed maps and model simulations. *Journal of Geophysical Research: Planets*, *125*(8), e2019JE006111. <https://doi.org/10.1029/2019JE006111>
- Neary, L., Daerden, F., Aoki, S., Whiteway, J., Clancy, R. T., Smith, M., et al. (2019). Explanation for the increase in high altitude water on Mars observed by NOMAD during the 2018 global dust storm. *Geophysical Research Letters*, *47*(7), e2019GL084354. <https://doi.org/10.1029/2019GL084354>
- Pätzold, M., Tellmann, S., Häusler, B., Hinson, D., Schaa, R., & Tyler, G. L. (2005). A sporadic third layer in the ionosphere of Mars. *Science*, *310*(5749), 837–839. <https://doi.org/10.1126/science.1117755>
- Plane, J. M. C. (1991). The chemistry of meteoric metals in the Earth's upper atmosphere. *International Reviews in Physical Chemistry*, *10*(1), 55–106. <https://doi.org/10.1080/01442359109353254>

- Plane, J. M. C., Carrillo-Sanchez, J. D., Mangan, T. P., Crismani, M. M. J., Schneider, N. M., & Määttänen, A. (2018). Meteoric metal chemistry in the Martian atmosphere. *Journal of Geophysical Research: Planets*, *123*(3), 695–707. <https://doi.org/10.1002/2017JE005510>
- Plane, J. M. C., Feng, W., & Dawkins, E. C. M. (2015). The mesosphere and metals: Chemistry and changes. *Chemical Reviews*, *115*(10), 4497–4541. <https://doi.org/10.1021/cr500501m>
- Plane, J. M. C., Flynn, G. J., Määttänen, A., Moores, J. E., Poppe, A. R., Carrillo-Sanchez, J. D., & Listowski, C. (2017). Impacts of cosmic dust on planetary atmospheres and surfaces. *Space Science Reviews*, *214*(1), 23. <https://doi.org/10.1007/s11214-017-0458-1>
- Schneider, N. M., Deighan, J. I., Jain, S. K., Stiepen, A., Stewart, A. I. F., Larson, D., et al. (2015). Discovery of diffuse aurora on Mars. *Science*, *350*(6261), aad0313. <https://doi.org/10.1126/science.aad0313>
- Schneider, N. M., Deighan, J. I., Stewart, A. I. F., McClintock, W. E., Jain, S. K., Chaffin, M. S., et al. (2015). MAVEN IUVS observations of the aftermath of the Comet Siding Spring meteor shower on Mars. *Geophysical Research Letters*, *42*(15), 4755–4761. <https://doi.org/10.1002/2015GL063863> @ 10.1002/(ISSN)1944-8007.COMET1
- Schneider, N. M., Jain, S. K., Deighan, J., Nasr, C. R., Brain, D. A., Larson, D., et al. (2018). Global aurora on Mars during the September 2017 space weather event. *Geophysical Research Letters*, *45*(15), 7391–7398. <https://doi.org/10.1029/2018GL077772>
- Schneider, N. M., Milby, Z., Jain, S. K., González-Galindo, F., Royer, E., Gérard, J.-C., et al. (2020). Imaging of Martian circulation patterns and atmospheric tides through MAVEN/IUVS nightglow observations. *Journal of Geophysical Research: Space Physics*, *125*(8), e2019JA027318. <https://doi.org/10.1029/2019JA027318>
- Sliipski, M., Jakosky, B. M., Benna, M., Elrod, M., Mahaffy, P., Kass, D., et al. (2018). Variability of Martian turbopause altitudes. *Journal of Geophysical Research: Planets*, *123*(11), 2939–2957. <https://doi.org/10.1029/2018JE005704>
- Smith, P. L., Heise, C., Esmond, J. R., & Kurucz, R. L. (1995). *Atomic spectral line database*. Smithsonian Astrophysical Observatory.
- Stevens, M. H., Evans, J. S., Schneider, N. M., Stewart, A. I. F., Deighan, J., Jain, S. K., et al. (2015). New observations of molecular nitrogen in the Martian upper atmosphere by IUVS on MAVEN. *Geophysical Research Letters*, *42*(21), 9050–9056. <https://doi.org/10.1002/2015GL065319>
- Stevens, M. H., Siskind, D. E., Evans, J. S., Jain, S. K., Schneider, N. M., Deighan, J., et al. (2017). Martian mesospheric cloud observations by IUVS on MAVEN: Thermal tides coupled to the upper atmosphere. *Geophysical Research Letters*, *44*(10), 4709–4715. <https://doi.org/10.1002/2017GL072717>
- Streeter, P. M., Lewis, S. R., Patel, M. R., Holmes, J. A., & Kass, D. M. (2020). Surface warming during the 2018/Mars year 34 global dust storm. *Geophysical Research Letters*, *47*(9), e2019GL083936. <https://doi.org/10.1029/2019GL083936>
- Villanueva, G. L., Liuzzi, G., Crismani, M. M. J., Aoki, S., Vandaele, A. C., Daerden, F., et al. (2021). Water heavily fractionated as it ascends on Mars as revealed by ExoMars/NOMAD. *Science Advances*, *7*(7), eabc8843. <https://doi.org/10.1126/sciadv.abc8843>
- Whalley, C. L., & Plane, J. M. C. (2010). Meteoric ion layers in the Martian atmosphere. *Faraday Discussions*, *147*(0), 349–368. <https://doi.org/10.1039/C003726E>
- Withers, P., Mendillo, M., Hinson, D. P., & Cahoy, K. (2008). Physical characteristics and occurrence rates of meteoric plasma layers detected in the Martian ionosphere by the Mars Global Surveyor Radio Science Experiment. *Journal of Geophysical Research*, *113*(A12), A12314. <https://doi.org/10.1029/2008JA013636>
- Withers, P., Pratt, R., Bertaux, J. L., & Montmessin, F. (2011). Observations of thermal tides in the middle atmosphere of Mars by the SPICAM instrument. *Journal of Geophysical Research*, *116*(E11), E11005. <https://doi.org/10.1029/2011je003847>